

# Bioprinting of Stable Bionic Interfaces Using Piezoresistive Hydrogel Organoelectronics

Antonia Georgopoulou,\* Miriam Filippi, Lisa Stefani, Felix Drescher, Aiste Balciunaite, Arnaud Scherberich, Robert Katzschmann, and Frank Clemens\*

Bionic tissues offer an exciting frontier in biomedical research by integrating biological cells with artificial electronics, such as sensors. One critical hurdle is the development of artificial electronics that can mechanically harmonize with biological tissues, ensuring a robust interface for effective strain transfer and local deformation sensing. In this study, a highly tissue-integrative, soft mechanical sensor fabricated from a composite piezoresistive hydrogel. The composite not only exhibits exceptional mechanical properties, with elongation at the point of fracture reaching up to 680%, but also maintains excellent biocompatibility across multiple cell types. Furthermore, the material exhibits bioadhesive qualities, facilitating stable cell adhesion to its surface. A unique advantage of the formulation is the compatibility with 3D bioprinting, an essential technique for fabricating stable interfaces. A multimaterial sensorized 3D bionic construct is successfully bioprinted, and it is compared to structures produced via hydrogel casting. In contrast to cast constructs, the bioprinted ones display a high (87%) cell viability, preserve differentiation ability, and structural integrity of the sensor–tissue interface throughout the tissue development duration of 10 d. With easy fabrication and effective soft tissue integration, this composite holds significant promise for various biomedical applications, including implantable electronics and organ-on-a-chip technologies.

be useful for biomedical cell culture models and organ-on-a-chip systems for fundamental biological discovery, disease modeling, and pharmaceutical research.<sup>[4–7]</sup> With further development, sensorized bionic tissue will approach in vivo applications, such as cardiac bionic tissue pacemakers and neuroelectronic interfaces.<sup>[8]</sup>

For use in bionics, a sensor material should be biocompatible, retain its functionality within the chemical microenvironment of tissue and be flexible/stretchable to stably integrate within the surrounding tissue.<sup>[9–11]</sup> Biocompatible stretchable electronics, like soft sensor composites, are an emergent tool that can provide mechanically seamless integration with living tissue to measure deformation in situ.

Real-time monitoring of strain forces within the living tissue is vital for many applications.<sup>[12–13]</sup> Integrated sensing functions within engineered tissue can contribute to controlling tissue development processes in vitro.<sup>[16]</sup> Hydrogel materials are often used in the development of stretchable bioelectronics.<sup>[15–18]</sup> Specifically, synthetic hydrogels are popular for mechanical deformation sensing applications,

because of their capability to endure large elongation and long-term stability.<sup>[20–22]</sup>

However, synthetic hydrogels, like polyvinyl alcohol (PVA), are known to hinder cellular attachment and this is undesirable for

## 1. Introduction

Bionic or cyborg tissue combines electronics and living cells.<sup>[1–3]</sup> One category of bionic tissue consists of engineered tissue with integrated artificial sensors. This type of bionic tissue could

A. Georgopoulou, F. Clemens  
High Performance Ceramics Laboratory  
Empa  
Swiss Federal Laboratories for Material Science and Technology  
Dübendorf 8600, Switzerland  
E-mail: [antonia.georgopoulou@empa.ch](mailto:antonia.georgopoulou@empa.ch); [frank.clemens@empa.ch](mailto:frank.clemens@empa.ch)

M. Filippi, L. Stefani, F. Drescher, A. Balciunaite, R. Katzschmann  
Soft Robotics Laboratory  
Department of Mechanical and Process Engineering  
ETH Zurich  
Zurich 8092, Switzerland  
L. Stefani, A. Scherberich  
Department of Biomedicine  
University Hospital Basel  
University of Basel  
Basel 4031, Switzerland

 The ORCID identification number(s) for the author(s) of this article can be found under <https://doi.org/10.1002/adhm.202400051>

© 2024 The Authors. Advanced Healthcare Materials published by Wiley-VCH GmbH. This is an open access article under the terms of the [Creative Commons Attribution](https://creativecommons.org/licenses/by/4.0/) License, which permits use, distribution and reproduction in any medium, provided the original work is properly cited.

DOI: 10.1002/adhm.202400051

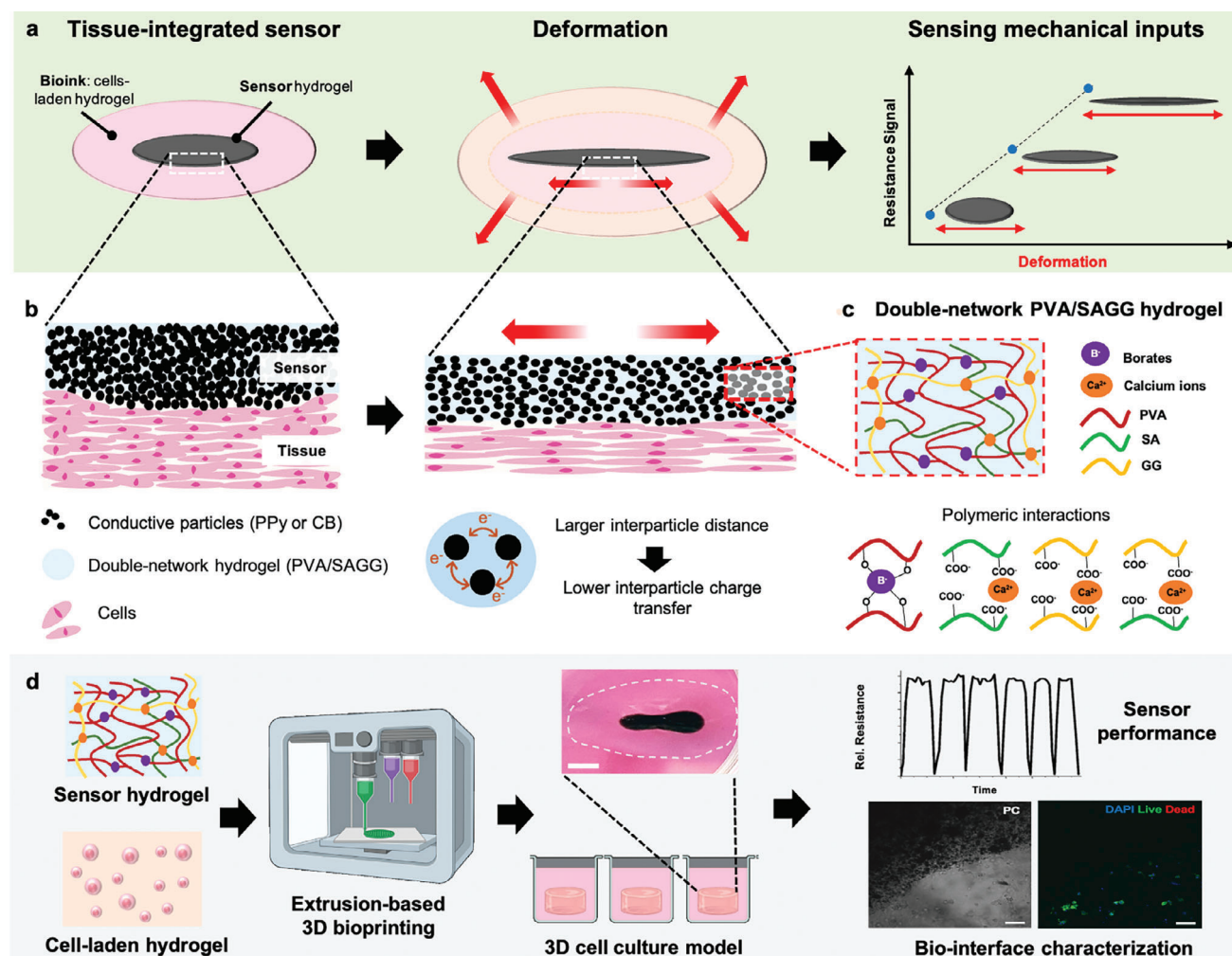


**Figure 1.** a) Scheme of the biphasic, bioprinted construct with a stable interface between the piezoresistive sensing ink and the cell-laden ink. b) Scheme of the sensing mechanism: the deformation is transferred from the soft tissue to the conductive double-network PVA/SAGG hydrogel through the stable interface. c) Scheme of the crosslinking mechanisms of the double network hydrogel, which increases the composite's stretchability and robustness. d) Scheme of the fabrication process of the sensorized, engineered tissue constructs: sensor ink and the bioink are coprinted, then cultured and finally tested for their sensor performance, biocompatibility, and structural integrity with coherent interfaces.

establishing stable bionic interfaces.<sup>[23,24]</sup> The disadvantage of natural-origin hydrogels is their poor mechanical properties, like the elongation at the point of fracture.<sup>[25,26]</sup> This is especially the case for composites where the addition of conductive fillers can result in embrittlement.<sup>[27–29]</sup> An alternative approach is to combine the synthetic hydrogel with a natural-origin hydrogel,<sup>[30–33]</sup> resulting in an interpenetrating polymer network composite, which combines the advantages of both types of component hydrogels.

Another challenge is achieving a stable interface between stretchable electronics and engineered soft tissue.<sup>[34,35]</sup> To monitor the strain levels accurately, soft tissue and sensing materials should seamlessly integrate and form a durable interface with minimized strain shielding effects, which reduce the accuracy of the mechanical deformation measurement.<sup>[36]</sup> As integrating conventional electronics in a preformed tissue can result in an unstable interface, fabrication of sensorized tissue should rely on designs and methods that minimize the risk of detachment of the sensor from the tissue surface.

Extrusion-based 3D bioprinting is an additive manufacturing method that enables the preparation of multimaterial tissue constructs, as it can deposit different materials (inks) with high space resolution in the same fabrication process.<sup>[37–40]</sup> With 3D bioprinting, one can manufacture constructs with complex designs and stable interfaces by tailoring the rheological properties of the different printed inks.<sup>[41–43]</sup> Interestingly, polymeric materials and their composites can be manufactured via 3D bioprinting.<sup>[44–46]</sup>

In this study, we manufacture a soft, printable piezoresistive sensor material by combining synthetic hydrogel PVA, natural-origin hydrogels sodium alginate (SA) and gellan gum (SAGG), and a conductive component, being either polymer polypyrrole (PPy) or carbon-based filler carbon black (CB). Multimaterial 3D bioprinting served to generate a 3D biphasic bionic structure, in which a living skeletal muscle tissue stably interfaces with the piezoresistive sensor (Figure 1a,b). We show that combining synthetic and natural polymers enhances the mechanical properties and biocompatibility of the resulting system. In particular,

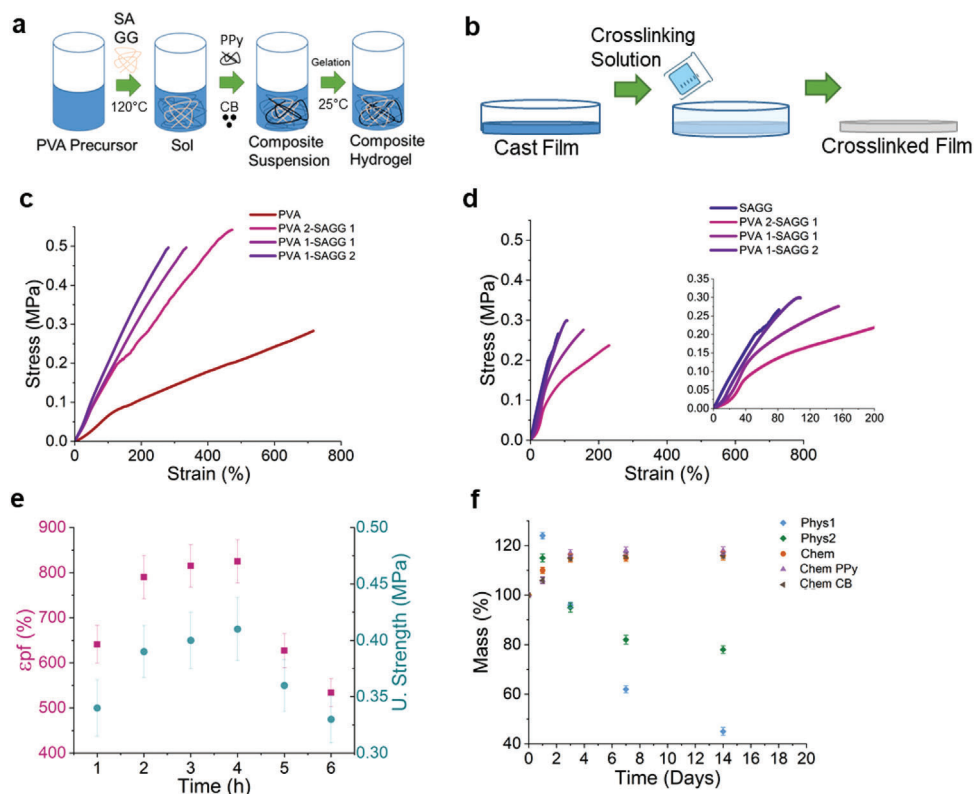


**Figure 2.** a) Synthesis steps of PVA-based hydrogel with PVA and SAGG. b) Synthesis steps of a double network hydrogel with PVA and SAGG. c) Stress–strain response for hydrogels with different ratios of PVA and SAGG crosslinked for 4 h with 10% w/v  $\text{CaCl}_2$  solution. d) Stress–strain response for hydrogels with different ratios of PVA and SAGG crosslinked for 4 h with 5% w/v  $\text{CaCl}_2$  solution/saturated  $\text{H}_3\text{BO}_3$ . e) The change in the elongation at the point of fracture (pf) and ultimate strength for the PVA 1:SAGG 2 hydrogel with varying crosslinking time. f) The mass change after exposure to the cell culture medium for PVA 1:SAGG 2 films crosslinked with exposure to 4 °C for 12 h (Phys1); exposure to –40 °C for 12 h (Phys2);  $\text{CaCl}_2$  5% w/v/saturated  $\text{H}_3\text{BO}_3$  solution for 4 h (Chem); and  $\text{CaCl}_2$  5% w/v/saturated  $\text{H}_3\text{BO}_3$  solution for 4 h in the presence of the PPy and CB fillers. All measurements represent the average of three samples.

the simultaneous physical and chemical crosslinking (Figure 1c) increases the material stretchability and preserves cell adhesion and survival. Finally, we use multimaterial 3D bioprinting to co-fabricate the sensing hydrogel composite with a bioink that contained muscle progenitor cells (Figure 1d). Thanks to the double network, the structural integrity of the interface is maintained over the 10 d required for the tissue maturation. Thus, we realized a sensorized bionic engineered tissue that could potentially in the future serve for future biomedical applications (such as intelligent implants, organ-on-a-chip devices, and biohybrid robots).

## 2. Results and Discussion

### 2.1. Characterization of the Double Network Hydrogels

Due to their ability to endure large deformation, synthetic hydrogels are often preferred in the development of piezoresistive sensors.<sup>[20,21]</sup> In this study, we investigated two different PVA-based composites with the conductive polymer PPy and CB fillers. As cellular adhesion is poor on pure PVA and its composites,<sup>[47,48]</sup> for use in cell culture models, the PVA is typically combined with natural-origin polymers.<sup>[23]</sup> Here, we enriched PVA with SA, a natural polymer that is also used for the

development of cell-laden bioinks. In addition, GG was used as a rheological agent to increase the viscosity of the composite for the 3D printing processing.

To identify an optimal ratio between the composite components, we first investigated the tensile properties of the polymer hydrogel in the absence of the fillers. A tensile test to the point of fracture (pf) was performed on polymer formulations that were based on different ratios of PVA and SAGG and then stabilized via different crosslinking protocols. Reducing temperature (from 120 to 25 °C) during the hydrogel preparation induced a primary physical crosslinking in the polymer network (Figure 2a).<sup>[49,50]</sup> In addition, we induced a secondary crosslinking by immersing the hydrogels in an ionic solution (Figure 2b). In particular, PVA was chemically crosslinked via an esterification reaction with boric acid ( $\text{H}_3\text{BO}_3$ ), while calcium chloride ( $\text{CaCl}_2$ ) was used to trigger ionic crosslinking to SAGG by interchain ionic interactions.<sup>[51–53]</sup> We compared a 10% w/v  $\text{CaCl}_2$  solution and a 5% w/v  $\text{CaCl}_2$  solution in saturated  $\text{H}_3\text{BO}_3$ . Figure 2c–e shows the mechanical properties of pure PVA and PVA with the SAGG mixtures.

Analyzing the effects of the two different crosslinking solutions on the mechanical properties of the polymer matrix (Figure 2c,d), we found that crosslinking with the 10% w/v  $\text{CaCl}_2$  solution significantly lowered the tensile strength for all compositions (<0.3 MPa). The pure SAGG composition displayed a low

elongation at the pf (60%), which is unsuitable for stretchable electronic applications. Upon the addition of the PVA polymer (1 PVA:2 SAGG mass ratio), the elongation at the pf and ultimate strength improved only to a minor extent (18%), whereas a much larger PVA content (2 PVA:1 SAGG mass ratio) was required to increase the elongation up to 100%.

When the 5% w/v  $\text{CaCl}_2$ /saturated  $\text{H}_3\text{BO}_3$  crosslinking solution was used, the pure PVA displayed a large elongation at the pf (680%). By adding the SAGG, the elongation of the pf decreased and the ultimate strength increased, possibly due to the reduction of the relative content of the highly elastic PVA. Double network hydrogels are known for their stability and good mechanical properties, like the ultimate strength of the composite.<sup>[54,55]</sup> Only a slight reduction in the ultimate strength (0.04 MPa) was observed for the hydrogel with the highest SAGG content (PVA1-SAGG2). Crosslinking with the 5% w/v  $\text{CaCl}_2$ /saturated  $\text{H}_3\text{BO}_3$  solution led to formulations that contained higher SAGG amounts and thus could apply to stretchable electronic systems. To identify the optimal crosslinking time with the 5% w/v  $\text{CaCl}_2$ /saturated  $\text{H}_3\text{BO}_3$  solution, the cast films were immersed for different time ranges in the solution before performing the tensile test (Figure 2e). As a crosslinking procedure exceeding 4 h led to the film embrittlement and the loss of mechanical performance, such a crosslinking duration was applied to achieve the highest elongation at the pf and the ultimate strength.

As we expected absorption of the aqueous medium from our hydrogel and possible PVA dissolution,<sup>[56,57]</sup> we tested if the cast hydrogel could retain structural integrity when placed in wet biological systems (such as the cell culture environment). We immersed physically and chemically crosslinked films in the cell culture medium and monitored their mass change over time (Figure 2f). After 24 h of incubation, films based on all the different hydrogel formulations showed a positive mass change. However, the mass change degree was smaller for the films crosslinked with the 5% w/v  $\text{CaCl}_2$ /saturated  $\text{H}_3\text{BO}_3$  solution (Chem) as compared to the samples with sole physical crosslinking, which started to dissolve after 3 d of incubation. The mass gradually decreased with time, with more evident effects for films crosslinked at 25 °C (Phys1) and smaller effects for samples that were crosslinked at -40 °C (Phys2). Importantly, the films crosslinked with the 5% w/v  $\text{CaCl}_2$ /saturated  $\text{H}_3\text{BO}_3$  solution did not dissolve in two weeks of observation, and after an initial mass increase, their mass remained unaltered after 3 d. Finally, adding the conductive fillers (PPy or CB) did not alter the composite stability within the cell growth medium (GM).

## 2.2. Biocompatibility of the Sensing Ink

To test whether the sensor hydrogel formulations could be used in biomedical applications, their biocompatibility was investigated on cells grown in 2D and 3D models. First, the biocompatibility tests were carried out on monolayers (Figure 3a) of different cell types, including fibroblasts (NIH 3T3), macrophages (RAW 264.7), motor neuron-like cells (NSC-34), and myoblasts (C2C12). Varying concentrations of PVA/SAGG-based hydrogels with or without CB or PPy were added to the cell culture media and cell viability was quantified via Resazurin assay after different time ranges (1, 3, 6, and 24 h) (Figure 3b,c, and Figures S1 and

S2, Supporting Information). Whereas no statistically relevant difference was found among the different cell type's responses, a mild cell viability decrease was observed when the cells were exposed to the highest material concentrations (10 and 100 mg mL<sup>-1</sup>) and for the longest time range (24 h) (Figure 3b,c). Nevertheless, for any tested incubation condition and cell type, the overall cell viability was higher than 80%, suggesting that neither the hydrogel nor its combination with the two filler types was cytotoxic. Overall, non-crosslinked sensor hydrogel formulations were biocompatible with different cell types including bioelectric cells such as muscle cells and motor neurons that are useful for bionic constructs manufacturing. Similar concepts have been exhibited with bionic structures with integrated EMG electrodes<sup>[58]</sup> and bionic tissue engineering with integrated electronics that apply mechanical cues for supporting tissue growth.<sup>[59]</sup> These examples show the great potential of bionic tissue, however integrated sensing was not yet explored and could offer additional benefits for monitoring and modeling tissue functions.

Second, we tested the cell viability after embedding the cells within 3D cell culture systems (Figure 3a) based on the PVA-SAGG hydrogel formulation that was crosslinked with 5% w/v  $\text{CaCl}_2$ /saturated  $\text{H}_3\text{BO}_3$  solution. To fabricate these systems, we co-assembled myoblast cells with the double-network sensing hydrogel and quantified the cell viability via Live/Dead by confocal microscopy analysis after 2 d of cell culture (Figure 3d).

The viability of cells embedded in these hydrogels was ≈45% and 50%, thus less than the cell viability index calculated when dissolving non-crosslinked hydrogels into the media (Figure 3b,c). The viability of cells embedded in the sole SAGG and PVA/SAGG formulations was very high (around 95% and 87%, respectively), confirming the suitability of these materials to realize mm-scale cell culture models.

Interestingly, embedding the cells in pure PVA resulted in a consistent cell viability decrease (<20%) with cells appearing sparser than in the control conditions (Figure 3e,f), which suggests the occurrence of consistent cytotoxicity effects. To understand if crosslinked hydrogels could serve as a substrate surface for cell growth, we then seeded cells on top of mm-thick crosslinked PVA and PVA/SAGG layers. While after 1 d of incubation, cells could not be found on the PVA construct surface, cell adhering and growing were observed on crosslinked PVA/SAGG surface.

We concluded that even if pure PVA hydrogels do not enable proper cellular adhesion, PVA/SAGG-based composite could be used in 3D cell culture systems. Upon the addition of a conductive filler, the viability decreased to 60% for the CB and 50% for the PPy. Thus, to best preserve cell viability, embedding the cells within the matrix should be avoided. The composite could participate in the composition of a 3D cell culture system but without incorporating the cells, rather being an integrated element of the cell culture system.

## 2.3. Mechanoelectrical Characterization of the Double-Network Hydrogel Composites

To describe the mechanoelectrical properties of the double-network hydrogel formulation, we investigated the effects of the

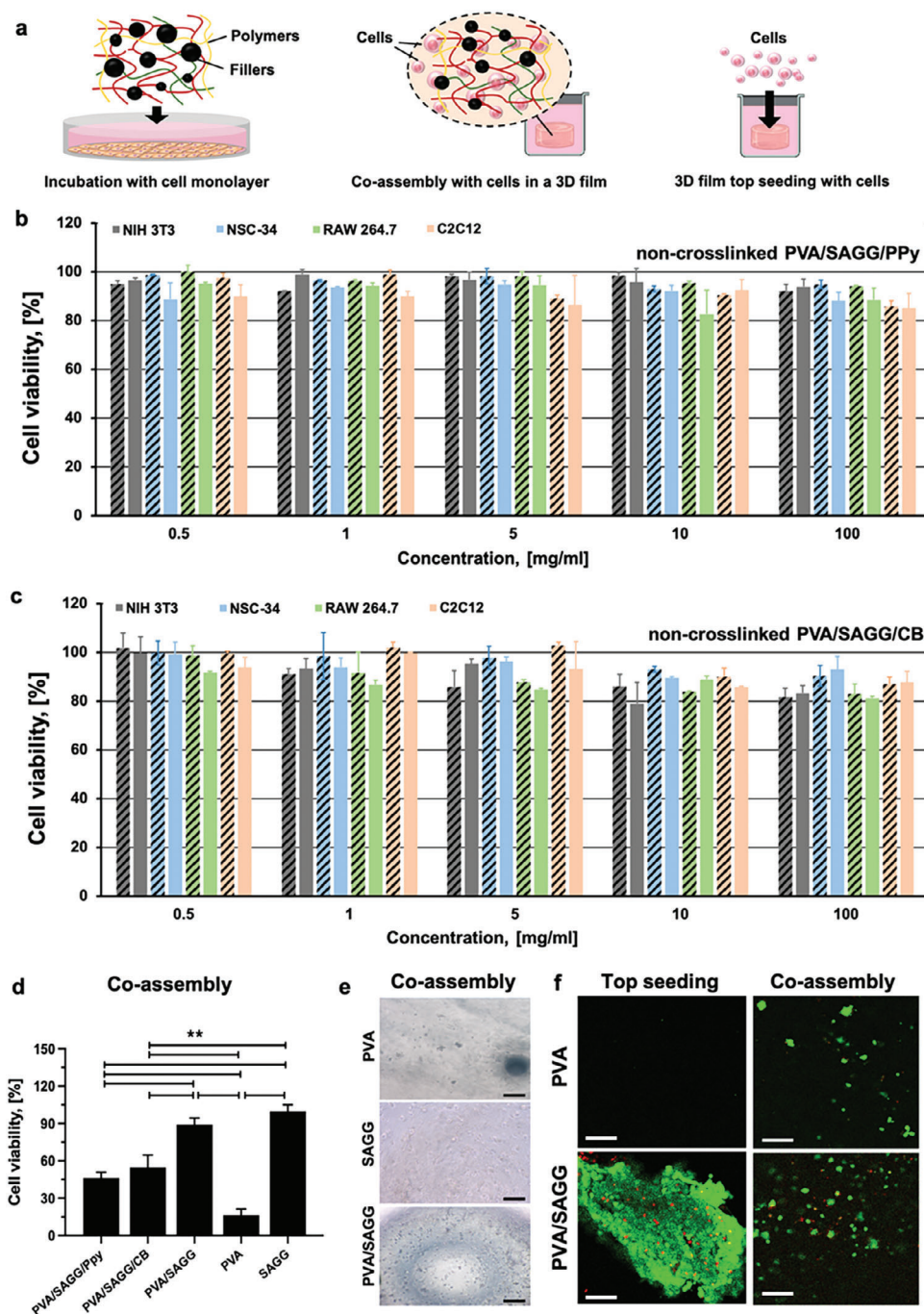


**Figure 3.** a) Configurations for co-assembly and top-seeding experiments. Cell viability calculated as a percentage from Resazurin viability tests of different cell lines including murine fibroblast (NIH 3T3), neuroblastoma cells (NSC-34), macrophages (RAW 264.7), and myoblasts (C2C12) that were exposed for 24 h to variable concentrations of PVA-SAGG doped with b) CB and c) PPy dissolved in the cell culture medium. Patterned and nonpatterned bars refer to fillers-enriched hydrogels and control formulations (no fillers), respectively. Viability data were represented as average from four technical replicates in three experimental replicates. d) Percentage cell viability of C2C12 cells that were co-assembled with different hydrogel formulations enriched with SAGG, CB, and PPy. The mass ratio between PVA and SAGG was 1:2. Cell viability data were expressed as average from three experimental replicates performed on two technical replicates. Statistical significance (one-way ANOVA) is expressed as \* for  $p < 0.05$ , \*\* for  $p < 0.01$ , and \*\*\* for  $p < 0.001$ . e) Optical microscopy of cells embedded in PVA, SAGG, and PVA/SAGG hydrogels, scale bars: 100  $\mu\text{m}$ . f) Confocal imaging of C2C12 cells tested via Live/Dead assay after seeding onto or into 3D hydrogel constructs (left and right, respectively), scale bars: 50  $\mu\text{m}$ .

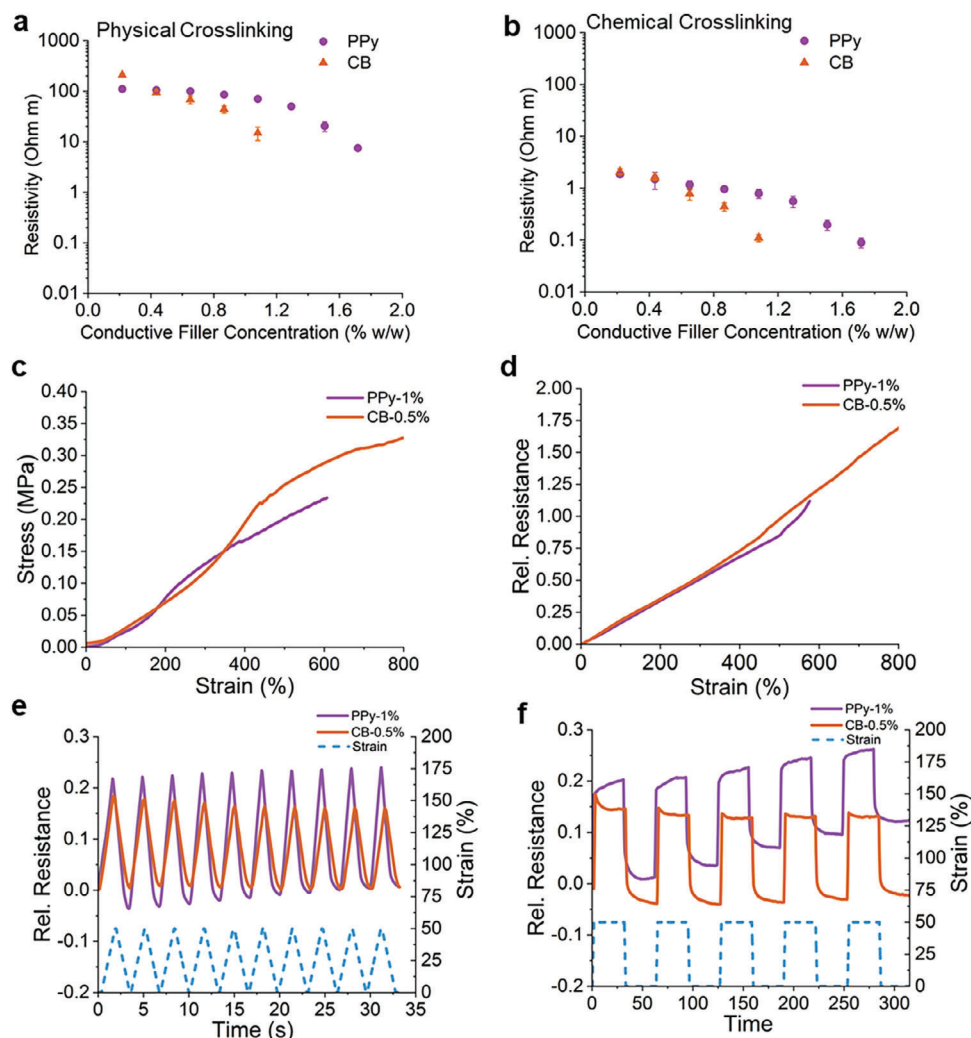


**Figure 4.** a) Change in the resistivity of the PVA 1:SAGG 2 hydrogel with the conductive filler content (1% w/v PPy or 0.5% w/v CB) after physical crosslinking by exposure to  $-40\text{ }^{\circ}\text{C}$  for 12 h and b) crosslinking with 5% w/v  $\text{CaCl}_2$ /saturated  $\text{H}_3\text{BO}_3$  solution for 4 h. c) Stress–strain response, d) resistance–strain response, e) dynamic signal response, and f) quasi-static signal response for the PVA 1:SAGG 2 film with 1% w/v PPy and 0.5% w/v CB after crosslinking with a saturated  $\text{H}_3\text{BO}_3$  solution for 4 h. All measurements represent the average of three samples.

chemical crosslinking and also those of the physical crosslinking that was triggered by cooling down the hydrogel from  $120\text{ }^{\circ}\text{C}$  to room temperature. In particular, by comparing the resistivity values of the material subjected to physical crosslinking and the secondary chemical crosslinking with 5% w/v  $\text{CaCl}_2$ /saturated  $\text{H}_3\text{BO}_3$  solution (Figure 4a,b), we found that the resistivity was showed a 100-fold increase after the secondary crosslinking. We attributed this change to the addition of ions during the chemical crosslinking. By increasing the CB content, the composite resistivity decreased. However, CB content higher than 0.5% w/w led to inhomogeneous mixing and the formation of large CB agglomerates that resisted the shear stress generated during the mixing. The resistivity was reduced with increasing PPy concentration, but higher PPy concentration (up to 1% w/w) could not be efficiently mixed. For higher PPy concentrations, the viscosity significantly increased, impairing the homogeneous mixing and limiting the potential of these formulations for further extrusion-based bioprinting applications.

Adding the fillers to the double-network hydrogel also increased the elongation at the pf of the composite film. Such an effect was already reported for hydrogel-based systems and is likely due to the reinforcing effect of the additives on the polymeric network.<sup>[60,61]</sup> Filling the polymer composite with 1% w/v of PPy resulted in a 24% lower tensile modulus as compared to using 0.5% w/v CB, possibly due to the lower filler content (Figure S3, Supporting Information). Compared to other formulations based on SA,<sup>[62–64]</sup> our composition had an elongation at break above 200% (Figure 4c). This area of strains suggest a broad application potential, even for systems that require extreme flexibility, like e-skin. With any of the filler types, composites displayed a monotonic sensor signal response at low strains (Figure 4d). Below 300% strain, the slope of the relative resistance–strain curve, which is an indicator of the sensitivity of the sensor response, remained unaltered. To compare the resistivity between the composites, the Gauge factor (GF) was calculated at 100% strain. The GF was 0.28 and 0.31

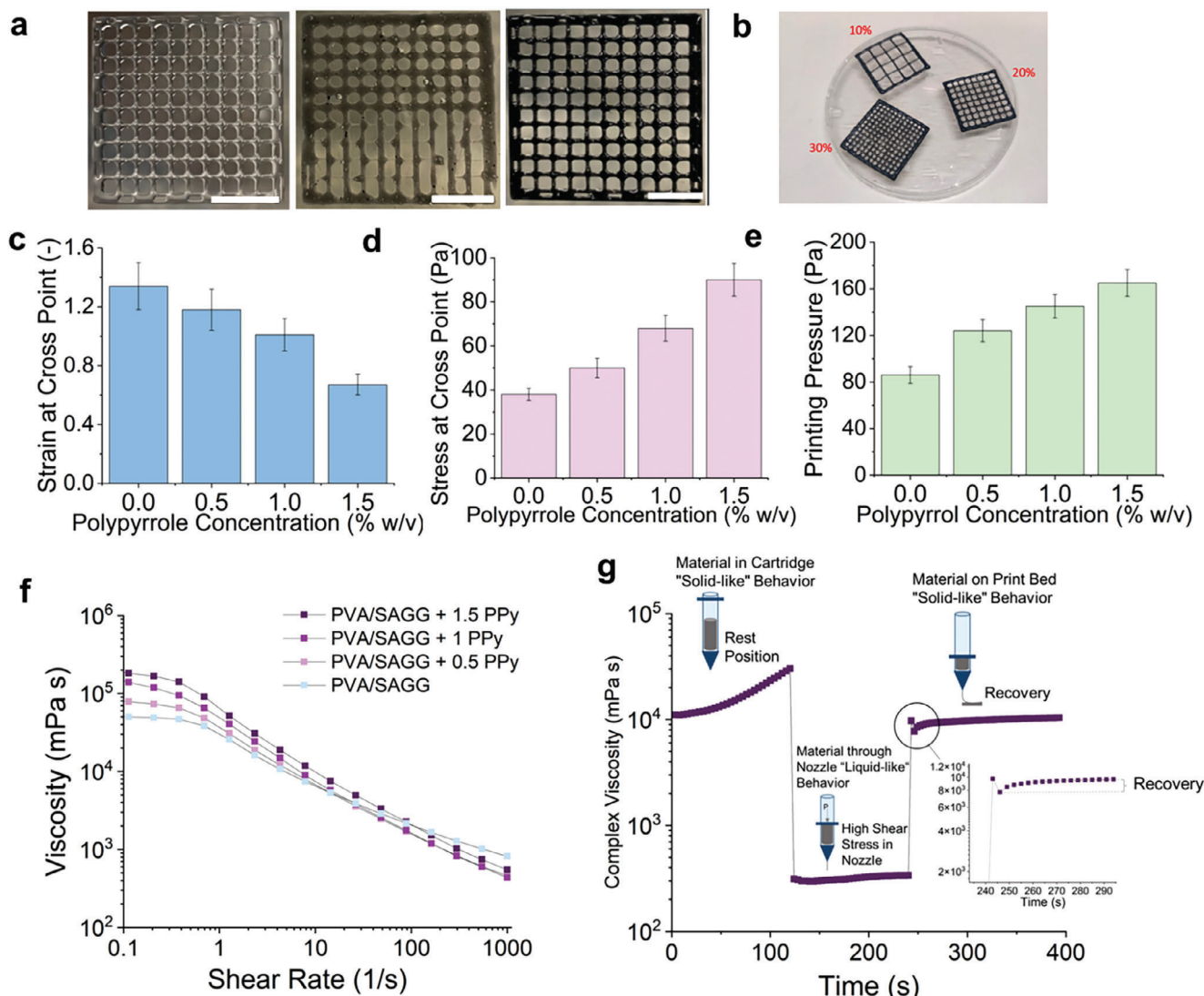


**Figure 5.** a) Optical pictures of two-layer grids with 20% infill fabricated with extrusion-based 3D printing with the PVA 1:SAGG 2 hydrogel without the filler (left), with 0.5% w/v CB (middle), and PPy 1% w/v (right). Scale bars: 1 cm. b) Representative pictures of the bilayered grids with 10%, 20%, and 30% infill designs fabricated with the PPy-based sensor hydrogel. c) The strain and d) stress calculated by the cross-over for  $G'$  and  $G''$  during the oscillatory amplitude sweep tests (Figure S4, Supporting Information) and e) pressure used during the biofabrication process for sensor hydrogel with different PPy contents. f) Shear-thinning curve for the PPy-based sensor hydrogel with variable filler concentrations. g) Shear recovery curve for the 1% w/v PPY-based sensor hydrogel. All measurements represent the average of three samples.

for the composition with PPy and CB, respectively, showing only a minimal difference between the two filler types.

We investigated the mechano-electrical properties of the composite films under dynamic and quasi-static cycling conditions, as reported by Georgopoulou et al.<sup>[65,66]</sup> In dynamic cycling tests (Figure 4e), we found that relative resistance, i.e., sensitivity of the CB composites, decreased with the number of cycles. Between the second and last cycle, a drift in the relative resistance ( $\approx 12\%$ ) occurred. A more stable response was recorded for the PPy composites at maximum strain, leading to a smaller drift ( $\approx 2\%$ ). At minimum strain, both composites exhibited a drift of 1% and 6% for the CB and PPy, respectively. In a quasi-static test (Figure 4f), the two composites displayed similar ranges of electrical signal relaxation ( $\approx 18\%$ ), but with a negative and posi-

tive drift over the cycle number for CB and PPy, respectively. The value of the drift confirmed the calculations performed during the dynamic test.

#### 2.4. 3D Printing and Rheological Characterization of the Double Network Hydrogel Composites

To understand if the selected conductive composite hydrogels could serve as printable inks for extrusion-based 3D printing, we printed a grid with 20% infill. A control hydrogel with no filler was used to validate the printing of the grid structure (Figure 5a, left). Printing a grid with 20% infill rounded corners appeared. The extrusion of the CB-composite was arduous and only the

printing of the first grid layer could be completed, likely due to the formation of large CB agglomerates that clogged the extrusion nozzles (Figure 5a, middle). The edges of the grids that were printed with PPy-composites were more accurately printed than those of the control hydrogels (Figure 5a, right), suggesting adding certain conductive fillers increases the shape fidelity and printing quality, as reported elsewhere.<sup>[67]</sup> The ink spreading factor was  $34\% \pm 4$  and  $15\% \pm 1$  for the control and PPy composition, respectively. Considering ink spreading factors below 20% as indicators of high shape fidelity,<sup>[68–70]</sup> our composite proved to be printable with high shape fidelity. We also assessed the shape fidelity of bilayered PPy-composite grids printed with different designs (i.e., variable infill scheme, Figure 5b) and found that this composition enables the efficient realization of 3D print grids with infill up to 30% in which the spaces of the grid modules remained visible.

We rheologically characterized the PPy-composites with variable content of PPy. To understand if our hydrogel behaved like a viscoelastic fluid or a Newtonian liquid, we performed an amplitude sweep test with a rheometer operated under oscillatory mode and the amplitude (strain) of the applied oscillation increasing over time. With such a test, we estimated yield stress and strain by the crossover of  $G'$  (elastic modulus) and  $G''$  (viscous modulus) (Figure 5c). These two values indicate at which point the viscous part of the material dominates the rheological behavior (Figure 5d). We observed that higher filler concentration led to higher yield point values, which resulted in a higher pressure required for the extrusion of the sensor hydrogel during the 3D printing (Figure 5e). As the printing pressure required to extrude 1.5% PPy-composite almost matched the pressure limit supported by the printing device, to minimize extrusion inconsistency, we selected the 1% PPy-composite for further testing.

All the tested formulations, including the controls with no PPy, exhibited a shear-thinning behavior (Figure 5f). At low shear, the zero-viscosity increased with the PPy concentration. As the material shape fidelity and retention are crucial factors for fabricating multilayered structures, we investigated these properties in our sensor hydrogel formulation and thoroughly assessed its suitability for 3D printing fabrication. To estimate the transition time between “liquid-like” to a “gel-like” behavior of the composite, we performed a shear recovery test in which the rheometer was operated in alternated modes according to an oscillation–rotation–oscillation scheme (Figure 5g). For our formulation, we found a transition time of 20 ms. Such a short time indicates that our formulation could efficiently recover its shape during the printing process and was linked with the good shape fidelity observed during the 3D bioprinting of the grid structure.

## 2.5. Bioprinting and Assessment of the Bionic Interfaces

To test whether the sensing hydrogel could integrate into 3D cell culture models, we printed it together with a cell-laden hydrogel (bioink) via multimaterial 3D bioprinting, aiming at generating a biphasic tissue construct with a living tissue layer and the sensor hydrogel in its center (Figure 6a). The living tissue was generated from a myoblast cells-laden bioink and the whole construct was cultured in conditions that supported cell differentiation into skeletal muscle tissue. As designed in the

cm-scale (i.e., length  $\approx 2.5$  cm), our biphasic construct could be realized in six-well plates with a rapid printing procedure ( $<30$  s per construct), which suggested that rapid production cycles could be carried out. As evaluated by Live/Dead assay, the postprinting cell viability was high (above 80%) and remained comparable to cell viability of control constructs that were realized via the manual deposition of the inks. As compared to construct designs in which the two materials were simply juxtaposed (e.g., layers' overimposition), depositing the materials with a core–shell design provided higher mechanical stability to the assembly (Figure S5, Supporting Information). As the forces arising within a 3D hydrogel cell culture model during its maturation (i.e., hydrogel shrinking, tissue remodeling, and the induced mechanical tensioning from tissue maturation protocols) follow a concentric directionality, they likely favor cohesion of the two materials in core–shell designs, but not in others, such as juxtaposed layers (Figure S6, Supporting Information).

Unlike previous studies where cells were seeded on top of 3D printed constructs,<sup>[71,72]</sup> we cofabricated tissue and sensors with a time-efficient, one-step process. The multimaterial 3D bioprinting approach allowed us to precisely deposit the hydrogel-based inks and generate a sensorized living tissue, in which the soft sensor and the cellularized hydrogel stably interfaced through all the tissue maturation process ( $\approx 10$  d) and along the whole interface length. Viable cells were observed within the bioink-printed area, as well as in direct contact with the sensor hydrogel (Figure 6c). Moreover, the biphasic hydrogel construct retained its shape and co-assembled state over time (Figure 6d left). When manufactured via bioprinting, the constructs featured a coherent interface between the living tissue and the sensor materials, with extended areas of adherence. In contrast, when fabricated via manual hydrogel casting, the constructs displayed extended no-contact areas between the two materials, mostly due to the imprecision of the fabricator's ability-dependent process (e.g., the presence of air bubbles or inaccurate deposition). Thus, we concluded that, due to its precision and high spatial control, the 3D printing process elicits the deposition of hydrogels with high accuracy and space resolution, and enhances the outcome of the co-assembly process (Figure 6e). Overall, these results indicate that our sensorized tissue model can be fabricated in a biocompatible, high method.

To test the functionality of the printed sensing ink in the biphasic 3D cell culture model, we kept the constructs in culture for two weeks to reach full tissue maturation and then we mechanically stressed them by exerting tension on their side borders and then we measured the relative resistance change in response to the induced structural deformation (Figure 6e). The relative resistance varied linearly with the percentage deformation, suggesting that the sensor hydrogel retained its sensor properties after tissue fabrication and maturation. By repeating the mechanical stress through consecutive cycles of compression–relaxation (Figure 6f), the relative resistance varied according to the applied stimulation schemes, displaying peaks of resistance values during the applied deformation. Moreover, during tissue maturation, no detachment or changes across the interface were observed, thus demonstrating the robustness of the co-assembled system. Based on these results, we concluded that the sensor hydrogels can reliably perform when fabricated in multi-

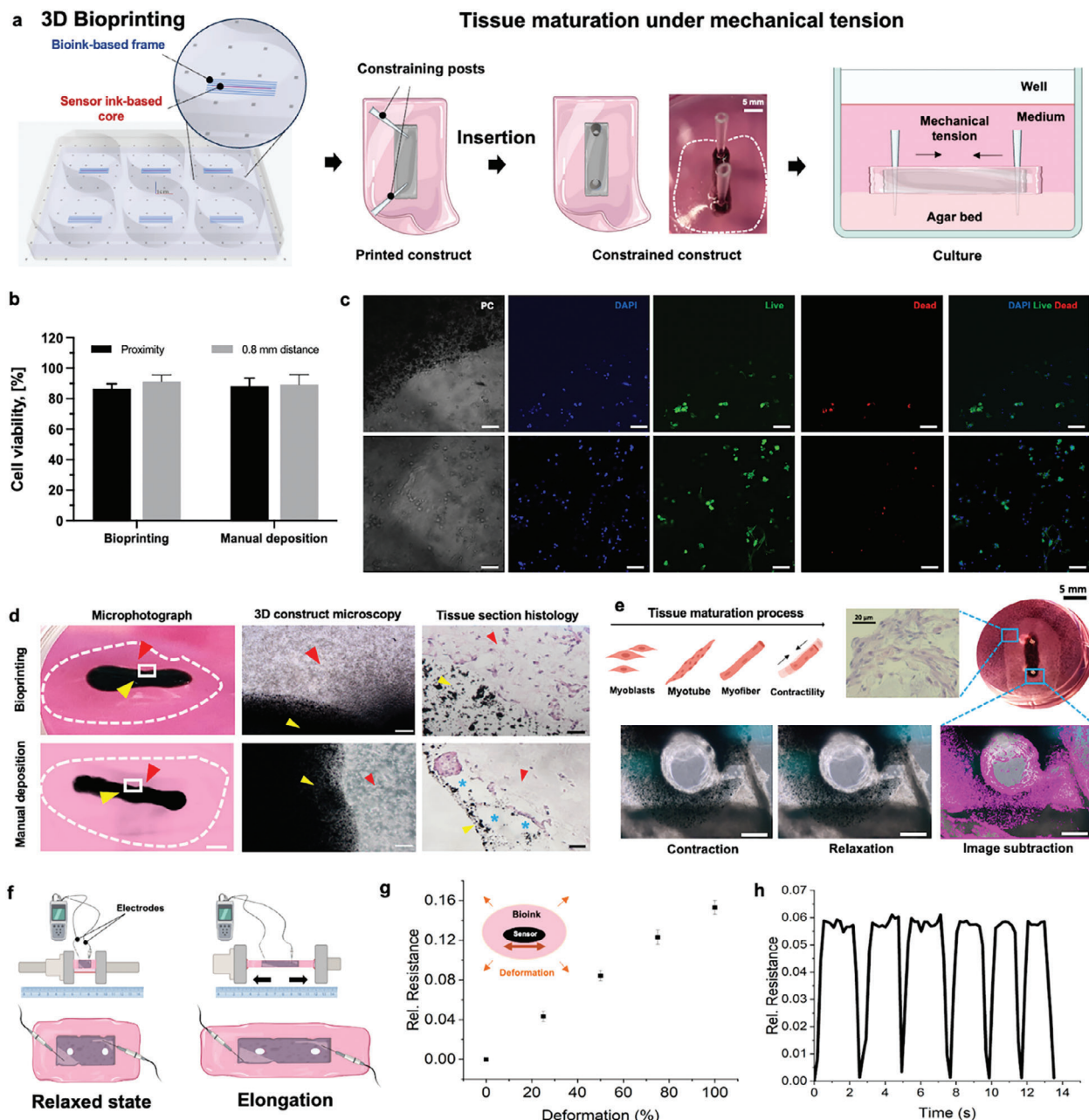


**Figure 6.** a) Schematics of the biofabrication process of the 3D bioprinting scheme. Design of a 3D tissue construct incorporating the sensor hydrogel within the construct core. Printing scheme for direct fabrication of one-layered, dual-material constructs, and the printing scheme for its multimaterial bioprinting fabrication in six-well plates (left). Insertion of posts as mechanical constraints to allow the sensorized 3D cell culture models to mature into tissue under mechanical tension (middle). Schematics (lateral view) of the culture well with the construct fixed to an agar bed and submerged in culture medium (right). b) Percentage cell viability immediately after construct printing in the proximity (top) and at 0.8 mm of linear distance (bottom) from the interface with the sensor hydrogel, as measured via confocal imaging of 3D constructs stained with Live/Dead assay. Data were averaged from three experimental replicates performed on three technical replicates. A paired Student *t*-test was applied against “manual deposition” as a control condition. c) Representative pictures of confocal imaging of constructs shown in phase contrast (PC, grays), nuclear staining (DAPI, blue), live and dead cells (green and red, respectively), and merged fluorescence. Scale bars: 50  $\mu\text{m}$ . d) Optical imaging of the 3D bioprinted model and its tissue sections after 10 d of cell culture. Red and yellow arrows indicate the cell-laden and sensor hydrogels, respectively. Blue asterisks highlight void areas that indicate detachment of the two materials and a fragile interface. Scale bars: 2 mm, 200  $\mu\text{m}$ , and 50  $\mu\text{m}$  for microphotography, 3D construct and tissue section microscopy, respectively. e) Top: schematics of the tissue maturation process leading to contractile functions of the muscle tissue (left); H&E staining of the formed myofibers (middle) and microscopic pictures of a matured construct (right). Bottom: construct’s detail during a contracted and relaxed state of the engineered skeletal muscle tissue (left and middle), and image subtraction of the two pictures (right). Scale bars: 600  $\mu\text{m}$ . f) Schematics of the tensioning experiment and g) Relative resistance change in response to the variable percentage deformation induced by mechanical stimulation of the bioprinted constructs with the strain of 25%, 50%, 75%, and 100% applied and h) repeated mechanical stimulation over time (bottom). Data were calculated from three different samples.

material, co-integrated architectures, therefore it is a promising material for the fabrication of multifunctional engineered tissue constructs.

### 3. Conclusion

In our work, we developed soft, stretchable composites based on double-network hydrogels enriched with conductive fillers and we demonstrated their potential for building sensorized bionic structures to investigate local strains. We formulated a composite material with piezoresistive sensing functions that can be accurately 3D printed and co-integrated with biological materials to engineer complex tissue models that will serve for future biological modeling, pharmaceutical testing, and bionic implantable devices. Our composite formulation contained the synthetic polymer PVA that has advantageous mechanical properties, such as a high elongation at the point of fracture. The composite also included two natural polymers (SA and GG) that were added to enhance biocompatibility of the resulting material and formed a double-network polymer structure that was stabilized by two crosslinking mechanisms. The SA and GG enhanced cell viability, likely due to these natural polymers encouraging cellular adhesion.

Two different types of conductive fillers (PPy and CB) were used, but the resulting composites had similar sensor characteristics. The CB-composite exhibited a lower drift at small strains. Nonetheless, the CB tended to form agglomerates that reduced its applicability to additive manufacturing via extrusion-based 3D printing. Therefore, we selected the PPy-composite as a material with the potential for 3D fabrication of tissue-embedded sensors.

To achieve high and durable stability of the sensor hydrogel, we exploited chemical crosslinking so to enable the sensors' application to cell culture environments, which expose the composites to the cell culture medium, a regulated atmosphere composition, and a relatively high temperature (i.e., 37 °C for mammalian cell culture). By combining physical and chemical crosslinking strategies, we optimized the stability of the sensor hydrogel matrix and tuned its rheological behavior to maximize the material's printability and its ability to retain structural integrity. The sensor retained its functionality by providing a linear sensor response to the induced deformation. When we deformed the biphasic construct by applying a direct mechanical stimulus on the cell-laden compartment, we reported a linear dependency between the induced deformation and the sensor signal.

We then showed that the mechanical stimulus and resulting structural deformation could be sensed also in dynamic experiments, in which trains of stimuli are applied and resemble continuous motion patterns found in physiological phenomena (such as tissue pulsation or voluntary and involuntary contractions). In such experimental conditions, our 3D printable, soft hydrogel retained functionality within the biological environment and after exposure to repeated local, mechanical stresses. This observation points to their potential for various biomedical products including next-generation biological cell culture models or implantable systems for biometrics, diagnostics, or tissue regeneration.

### 4. Experimental Section

**Preparation of the Double Network Hydrogels:** PVA was purchased from Sigma Aldrich Chemie (Buchs, Switzerland) and dissolved in deionized water in concentration 12.5% w/v. After increasing the temperature to 90 °C, the solution was stirred for 1 h using a magnetic stirrer until its color changed from opaque white to translucent. At this state, SA (ThermoFischer Scientific, Reinach, Switzerland) and Phytigel (Sigma Aldrich Chemie, Buchs, Switzerland) were added and mixed under magnetic stirring for 1 h before cooling down again. The components were combined with different mass ratios (1:2, 1:1, 2:1).

To prepare the crosslinking solution, deionized water was used. Boric acid ( $H_3BO_3$ ) (ThermoFischer Scientific, Reinach, Switzerland) and calcium chloride ( $CaCl_2$ ) (ThermoFischer Scientific, Reinach, Switzerland) were used. Two different crosslinking solutions were assessed. The first solution contained a 5% w/v  $CaCl_2$  and saturated conditions for the  $H_3BO_3$ . The second solution contained a concentration of calcium chloride 10% w/v.

To prepare the composites, the conductive fillers PPy (Sigma Aldrich Chemie, Buchs, Switzerland), doped with 20% Ketjenblack EC-600JD CB (Lion Specialty Chemicals, Tokyo, Japan) were used. The conductive fillers were added to the double network hydrogel, and the composite was mixed with a high-speed mixer (Hauschild, Hamm, Germany) at 1500 rpm for 10 min.

**Cell Culture:** Different cell lines were used in this study: the murine myoblast cell line (C2C12), the macrophage cell line (RAW 264.7), and the fibroblast cell line (NIH/3T3) were obtained from the American Type Culture Collection (ATCC, Manassas, VA). The mouse motor neuron-like hybrid cell line (NSC-34) was purchased from Cedarlane Laboratories (via Tebu-Bio GmbH, Offenbach, Germany). Before use, cells were tested for mycoplasma (MycAlert Mycoplasma Detection Kit, Lonza AG, Basel, Switzerland). Cells were cultured in a monolayer at 37 °C in a 5%  $CO_2$ -containing humidified atmosphere in a complete GM. GM for myoblasts and macrophages consisted of Dulbecco's modified Eagle's medium (DMEM, #D6429, Sigma-Aldrich) supplemented with 10% (v/v) heat-inactivated fetal bovine serum (FBS, #F7524, Sigma-Aldrich),  $2 \times 10^{-3}$  M glutamine, 100 U  $mL^{-1}$  penicillin, and 100  $\mu g mL^{-1}$  streptomycin (all from ThermoFischer Scientific, Switzerland). GM for fibroblasts and motor neuron-like cells had the same formulation but with 10% (v/v) bovine calf serum (FCS, #N4637, Sigma-Aldrich) in the place of the FBS. For routine maintenance and expansion, the cells were seeded at an initial seeding density of  $5 \times 10^3$  cells  $cm^{-2}$  and detached from flasks by trypsinization (Trypsin EDTA 0.25%, Sigma-Aldrich) at 70% of cell confluency.

**3D Cell Culture Models:** To test the effects of the sensing ink components on cell viability, cells were co-assembled with the various hydrogel formulations to form mm-scale 3D cell culture models with a final volume of 100  $\mu L$  and seeded with  $5 \times 10^4$  cells each. Hydrogel formulations containing PVA and SA were crosslinked by adding 1 M boric acid and  $50 \times 10^{-3}$  M  $CaCl_2$ , respectively. After 5 min, the crosslinking solutions were removed and constructs were exhaustively washed with GM (at least 4 $\times$ , 200  $\mu L$  volume). To test the cells' ability to adhere to these materials, hydrogel layers of 100  $\mu L$  were crosslinked at the bottom of wells in 96-well plates. Before cell seeding, the constructs were washed with GM four times, and the well plates were sterilized under UV light for 30 min. Then, 100  $\mu L$  of GM mixed with 1.5 or  $20 \times 10^4$  cells were added on top of the hydrogel layers and left for 1 h in the cell culture incubator. Then, GM was slowly added to the wells (900  $\mu L$ ). After 24 h, cell viability in these constructs was investigated via Live/Dead staining and analysis in confocal microscopy.

**Biocompatibility Assessment of 2D Cell Cultures:** To evaluate cell survival and growth of cells cultured in 2D and then exposed to hydrogel formulation, the AlamarBlue assay was performed. Cells of different types were plated, and exposed to a cell culture medium in which various concentrations of PPy and CB-enriched PVA hydrogels were dissolved (concentration range: 0.5–100  $mg mL^{-1}$ ). Different exposure times were tested, including 1, 3, 6, and 24 h. Cells incubated with sole culture media or PVA with no fillers served as controls. At the end of incubation time, cells were washed with cell culture media (3 $\times$ ). Then, the culture medium was

supplemented with 10% (v/v) of AlamarBlue reagent solution at 0.1 mg mL<sup>-1</sup> (#R7017, Sigma-Aldrich) and incubated with cells at 37 °C for 2 h before the fluorescence signal (Ex/Em = 530/590) was measured with a Synergy H1 microplate reader (Biotek). Fluorescence intensity values were corrected for the background control (culture medium with resazurin). Cell viability was reported as a percentage with respect to values calculated for negative controls (cell incubated with sole culture media).

**Bioprinting:** All printed materials (i.e., cell-laden and sensing ink) were aseptically loaded into different cartridges. The inks were extruded through conical nozzles with an inner diameter of 410 μm (22G) (CELLINK, Boston, USA) in a closed aseptic chamber during the printing process. Before printing, the nozzles were aligned to determine their respective X-Y-Z offsets with a minimum 0.01 mm accuracy. Printing parameters were optimized against the following variables: pressure, speed, and temperature. The optimal printing conditions for each ink were determined through tests for strand assessment, printing accuracy, and shape fidelity. To create the bioink, the cells were counted, and a specific number of cells were centrifuged, collected as pellets, counted, and then mixed in a predetermined number with a certain biopolymer volume to generate the cell-laden bioink. The printing procedure was optimized to maximize the cell seeding density while retaining good mechanical properties of the resulting bioink that allowed for accurate printing. The optimal cell concentration was found to be 1 × 10<sup>6</sup> cells mL<sup>-1</sup>. To calculate the ink spreading factor in %, the difference of the diameter of a single printed line from the theoretical value (nozzle diameter) was divided with the theoretical value of a single line (nozzle diameter).

**3D Bioprinting and Culture of the Sensorized Muscle Tissue Constructs:** To realize the biphasic construct containing the sensing ink and myoblast-laden matrix, a G-Code to generate an inner line of sensing ink and a layer of bioink all around it was used. To realize the cell-laden part of the model, an extrudable mixture of Matrigel, collagen, and cells (concentration: 1 × 10<sup>6</sup> cells mL<sup>-1</sup>) was optimized. By manually depositing the inks according to the same scheme, internal controls useful to understand the effects of the bioprinting process were created. To mature the tissue under mechanical tension, as required per muscle tissue, the constructs were fixed through pillars to an agar bed (name, company, country) deposited at the bottom of the well, as previously reported. After printing, the myoblast-laden constructs were let into GM for 4 d to allow for cell proliferation. Half the volume of the culture media was collected and replaced with a new GM every day.

**Live/Dead Staining in 3D Constructs:** To assess cell viability in the constructs, Live/Dead staining was performed immediately after bioprinting following the manufacturer's instructions (Thermo Fisher Scientific; R37601). Calcein and propidium iodide were excited at 488 and 561 nm laser wavelengths, respectively, and imaged on a confocal microscope (Zeiss LSM 780 Airyscan, Zeiss AxioObserver.Z1).

**Histology:** After in vitro culture, the constructs were fixed overnight in a 4% paraformaldehyde solution at room temperature. Then, the samples were embedded in paraffin, and sections of 4.5 μm thickness were cut with a microtome (Microm, HM430, Thermo Scientific). The sections were stained with hematoxylin and eosin (#GHS116 and #HT110116, respectively, from Sigma-Aldrich). The slides were mounted and imaged in a bright field with a light microscope (Olympus CKX41, Olympus Schweiz AG).

**Mechanoelectrical Characterization:** Tensile testing was performed with a Zwick Roell Z005 universal testing machine (Zwick Roell, Ulm, Germany) with a strain rate of 200 mm min<sup>-1</sup>. Ten cycles of 0–50% strain were performed with a simultaneous recording of the electrical resistance with a source meter Keithley 2450 multimeter (Keithley Instruments, Solon, OH). A voltage of 1 V and a sampling rate of 10 Hz were used. The drift was calculated as the percentage difference of the relative resistance value at maximum strain between the second and last cycle, as described previously.<sup>[36,65]</sup> The GF was calculated as a measure of the piezoresistive sensor response sensitivity, by dividing the change of the relative resistance in a defined strain range with the strain range.

Mechanical tension was exerted on the 3D tissue constructs, while the electrical signal was recorded with time. A strain of 25%, 50%, 75%, and 100% was applied. The test was performed in a petri dish without addi-

tional anchoring of the constructs. The samples were immersed in a cell culture medium during the testing. Detailed information on the setup are shown in the Supporting Information.

**Rheological Characterization:** The rheological characterization was performed with a viscometer Anton-Paar MC302 (Anton Paar, Graz, Austria). A 20 mm parallel plate geometry was used with a bandgap of 0.5 mm for all rheological measurements. The complex viscosity was calculated with the RheoCompass software from Anton Paar. To analyze the complex viscosity, oscillation measurements were performed with 1 Hz oscillation frequency in the amplitude range between 0.1% and 100%. The shear thinning test was performed with a ramp shear rate 0.01–1000 s<sup>-1</sup> under rotational mode. The shear recovery was performed under oscillatory mode with 1 Hz oscillation frequency and 0.1% amplitude. After 120 s, the mode changed to rotational with a shear rate of 1000 s<sup>-1</sup>. After 120 s, the mode changed to oscillatory with 1 Hz frequency for 160 s.

**Statistical Analysis:** Mechanoelectrical and rheological characterization was performed for three samples. Data were presented as mean values – standard deviation with sample size ( $n = 3$ ). Statistical analysis was carried out using MS Excel Software. Biocompatibility was assessed by considering data acquired from at least three independent experiments and two technical replicates unless otherwise stated. Imaging analysis was performed on at least three images from each analyzed sample feature ( $\geq 3$  samples per condition;  $\geq 3$  experimental replicates). Measurements were taken from distinct samples unless otherwise stated in the text. Sample exclusion from experimental data collection or analysis was allowed when samples featured evident defects or damages compromising the experimental performance or validity (e.g., contaminated tissue samples). Two-sided Student's *t*-test was used to analyze cell viability in bioprinted constructs versus manual deposition control. One-way ANOVA was used to analyze cell survival within the scaffolds composed of different materials. Multiple comparisons between groups were performed with Tukey's post hoc test. Statistical significance is expressed as \* for  $p < 0.05$ , \*\* for  $p < 0.01$ , and \*\*\* for  $p < 0.001$ .

## Supporting Information

Supporting Information is available from the Wiley Online Library or from the author.

## Acknowledgements

This work was supported by the SHERO project, a Future and Emerging Technologies (FET) programme of the European Commission (Grant Agreement ID 828818) and by the Swiss National Science Foundation (SNSF) (Grant No. IZCOZO\_213312).

Open access funding provided by ETH-Bereich Forschungsanstalten.

## Conflict of Interest

The authors declare no conflict of interest.

## Data Availability Statement

The data that support the findings of this study are available from the corresponding author upon reasonable request.

## Keywords

bionic devices, bioprinting, hydrogels, sensing, stretchable electronics

Received: January 9, 2024

Revised: April 23, 2024

Published online:

- [1] T. Masuda, A. Menciassi, Q. Wang, *Adv. Rob.* **2019**, *33*, 207.
- [2] M. Guix, R. Mestre, T. Patiño, M. De Corato, J. Fuentes, G. Zarpellon, S. Sánchez, *Sci. Rob.* **2021**, *6*, abe75777.
- [3] J. Banks, A. P. Edwards, D. Westerman, *Cyberpsychol., Behav., Social Networking* **2021**, *24*, 324.
- [4] G. Orive, N. Taebnia, A. Dolatshahi-Pirouz, *Adv. Healthcare Mater.* **2020**, *9*, 1901023.
- [5] X. Duan, T.-M. Fu, J. Liu, C. M. Lieber, *Nano Today* **2013**, *8*, 351.
- [6] Y.-T. Kwon, Y.-S. Kim, S. Kwon, M. Mahmood, H.-R. Lim, S.-W. Park, S.-O. Kang, J. J. Choi, R. Herbert, Y. C. Jang, Y.-H. Choa, W.-H. Yeo, *Nat. Commun.* **2020**, *11*, 3450.
- [7] S. Agarwala, J. M. Lee, W. L. Ng, M. Layani, W. Y. Yeong, S. Magdassi, *Biosens. Bioelectron.* **2018**, *102*, 365.
- [8] Q. Li, K. Nan, P. Le Floch, Z. Lin, H. Sheng, T. S. Blum, J. Liu, *Nano Lett.* **2019**, *19*, 5781.
- [9] V. Magno, A. Meinhardt, C. Werner, *Adv. Funct. Mater.* **2020**, *30*, 2000097.
- [10] Z. Wang, H. Lin, M. Zhang, W. Yu, C. Zhu, P. Wang, Y. Huang, F. Lv, H. Bai, S. Wang, *Mater. Horiz.* **2023**, *10*, 1210.
- [11] A. Silvestri, C. Wetzl, N. Alegret, L. Cardo, H.-L. Hou, A. Criado, M. Prato, *Adv. Drug Delivery Rev.* **2022**, *186*, 114315.
- [12] S. Lee, D. Sasaki, D. Kim, M. Mori, T. Yokota, H. Lee, S. Park, K. Fukuda, M. Sekino, K. Matsuura, T. Shimizu, T. Someya, *Nat. Nanotechnol.* **2019**, *14*, 156.
- [13] X. Pei, H. Zhang, Y. Zhou, L. Zhou, J. Fu, *Mater. Horiz.* **2020**, *7*, 1872.
- [14] S. Liu, S. Kumari, H. He, P. Mishra, B. N. Singh, D. Singh, S. Liu, P. Srivastava, C. Li, *Biosens. Bioelectron.* **2023**, *231*, 115285.
- [15] Y. Leng, X. Li, F. Zheng, H. Liu, C. Wang, X. Wang, Y. Liao, J. Liu, K. Meng, J. Yu, J. Zhang, B. Wang, Y. Tan, M. Liu, X. Jia, D. Li, Y. Li, Z. Gu, Y. Fan, *Adv. Mater.* **2023**, *35*, 2211059.
- [16] E. Ferrari, C. Palma, S. Vesentini, P. Occhetta, M. Rasponi, *Biosensors* **2020**, *10*, 110.
- [17] C. Wang, T. Yokota, T. Someya, *Chem. Rev.* **2021**, *121*, 2109.
- [18] T. Wang, J. Song, R. Liu, S. Y. Chan, K. Wang, Y. Su, P. Li, W. Huang, *ACS Appl. Mater. Interfaces* **2022**, *14*, 14596.
- [19] X. Wu, H. Peng, *Sci. Bull.* **2019**, *64*, 634.
- [20] A. Georgopoulou, J. Brancart, S. Terryn, A. W. Bosman, S. Norvez, G. Van Assche, F. Iida, B. Vanderborcht, F. Clemens, *Appl. Mater. Today* **2022**, *29*, 101638.
- [21] U. S. K. Madduma-Bandarage, S. Madihally, *J. Appl. Polym. Sci.* **2021**, *138*, e50376.
- [22] L. Hu, P. L. Chee, S. Sugiarto, Y. Yu, C. Shi, R. Yan, Z. Yao, X. Shi, J. Zhi, D. Kai, H.-D. Yu, W. Huang, *Adv. Mater.* **2023**, *35*, 2205326.
- [23] J. Xie, D. Fan, *Int. J. Polym. Mater. Polym. Biomater.* **2020**, *69*, 928.
- [24] J. M. Ino, P. Chevallier, D. Letourneur, D. Mantovani, C. Le Visage, *Biomater* **2013**, *3*, e25414.
- [25] D. Zhang, B. Ren, Y. Zhang, L. Xu, Q. Huang, Y. He, X. Li, J. Wu, J. Yang, Q. Chen, Y. Chang, J. Zheng, *J. Mater. Chem. B* **2020**, *8*, 3171.
- [26] Y. Cai, J. Qin, W. Li, A. Tyagi, Z. Liu, M. Delowar Hossain, H. Chen, J.-K. Kim, H. Liu, M. Zhuang, J. You, F. Xu, X. Lu, D. Sun, Z. Luo, *J. Mater. Chem. A* **2019**, *7*, 27099.
- [27] C. Du, J. Hu, X. Wu, H. Shi, H. Chao Yu, J. Qian, J. Yin, C. Gao, Z. Liang Wu, Q. Zheng, *J. Mater. Chem. B* **2022**, *10*, 468.
- [28] C. Harito, D. V. Bavykin, B. Yuliarto, H. K. Dipojono, F. C. Walsh, *Nanoscale* **2019**, *11*, 4653.
- [29] X. Xiang, H. Li, Y. Zhu, S. Xia, Q. He, *J. Appl. Polym. Sci.* **2021**, *138*, 50801.
- [30] Q. Wei, R. Yang, D. Sun, J. Zhou, M. Li, Y. Zhang, Y. Wang, *J. Mater. Res. Technol.* **2022**, *17*, 66.
- [31] Y. Kan, A. I. Salimon, A. M. Korsunsky, *Mater. Today: Proc.* **2020**, *33*, 2013.
- [32] M. C. Catoira, L. Fusaro, D. Di Francesco, M. Ramella, F. Boccafoschi, *J. Mater. Sci.: Mater. Med.* **2019**, *30*, 115.
- [33] D. A. Gyles, L. D. Castro, J. O. C. Silva, R. M. Ribeiro-Costa, *Eur. Polym. J.* **2017**, *88*, 373.
- [34] R. Mestre, T. Patiño, S. Sánchez, *WIREs Nanomed. Nanobiotechnol.* **2021**, *13*, e1703.
- [35] M. Filippi, T. Buchner, O. Yasa, S. Weirich, R. K. Katzschmann, *Adv. Mater.* **2022**, *34*, 2108427.
- [36] A. Georgopoulou, S. Michel, B. Vanderborcht, F. Clemens, *Sens. Actuators, A* **2021**, *318*, 112433.
- [37] M. Rocca, A. Fragasso, W. Liu, M. A. Heinrich, Y. S. Zhang, *SLAS Technol.* **2018**, *23*, 154.
- [38] B. Grigoryan, D. W. Sazer, A. Avila, J. L. Albritton, A. Padhye, A. H. Ta, P. T. Greenfield, D. L. Gibbons, J. S. Miller, *Sci. Rep.* **2021**, *11*, 3171.
- [39] S. Agarwal, S. Saha, V. K. Balla, A. Pal, A. Barui, S. Bodhak, *Front. Mech. Eng.* **2020**, *6*, 589171.
- [40] N. Betancourt, X. Chen, *Bioprinting* **2022**, *25*, e00189.
- [41] M. Altunbek, F. Afghah, O. S. Caliskan, J. J. Yoo, B. Koc, *Biofabrication* **2023**, *15*, 022002.
- [42] W. Luo, H. Liu, C. Wang, Y. Qin, Q. Liu, J. Wang, *Adv. Eng. Mater.* **2019**, *21*, 1900019.
- [43] H. Wang, K. Guo, L. Zhang, H. Zhu, S. Li, S. Li, F. Gao, X. Liu, Q. Gu, L. Liu, X. Zheng, *Biofabrication* **2021**, *13*, 035001.
- [44] E. M. Euti, A. Wolfel, M. L. Picchio, M. R. Romero, M. Martinelli, R. J. Minari, C. I. A. Igarzabal, *Macromol. Rapid Commun.* **2019**, *40*, 1900217.
- [45] J. Xu, M. Zhang, W. Du, J. Zhao, G. Ling, P. Zhang, *Int. J. Biol. Macromol.* **2022**, *219*, 545.
- [46] D. Moura, R. F. Pereira, I. C. Gonçalves, *Mater. Today Chem.* **2022**, *23*, 100617.
- [47] C. Zhang, K. Liang, D. Zhou, H. Yang, X. Liu, X. Yin, W. Xu, Y. Zhou, P. Xiao, *ACS Appl. Mater. Interfaces* **2018**, *10*, 27692.
- [48] L. Sigurdson, D. E. Carney, Y. Hou, L. Hall III, R. Hard, W. Hicks Jr, F. V. Bright, J. A. Gardella, *J. Biomed. Mater. Res.* **2002**, *59*, 357.
- [49] J. M. Gohil, A. Bhattacharya, P. Ray, *J. Polym. Res.* **2006**, *13*, 161.
- [50] E. Rynkowska, K. Fatyeyeva, S. Marais, J. Kujawa, W. Kujawski, *Polymers* **2019**, *11*, 1799.
- [51] R. Dave, D. Madamwar, *Process Biochem.* **2006**, *41*, 951.
- [52] K. Bialik-Wąs, E. Królicka, D. Malina, *Molecules* **2021**, *26*, 2381.
- [53] H.-H. Wang, T.-W. Shyr, M.-S. Hu, *J. Appl. Polym. Sci.* **1999**, *74*, 3046.
- [54] A. A. Aldana, F. L. C. Morgan, S. Houben, L. M. Pitet, L. Moroni, M. B. Baker, *J. Polym. Sci.* **2021**, *59*, 2832.
- [55] Q. Chen, H. Chen, L. Zhu, J. Zheng, *J. Mater. Chem. B* **2015**, *3*, 3654.
- [56] X. Jiang, C. Li, Q. Han, *Polym. Bull.* **2023**, *80*, 1303.
- [57] D. Huang, Z.-D. Hu, Y. Ding, Z.-C. Zhen, B. Lu, J.-H. Ji, G.-X. Wang, *Polym. Degrad. Stab.* **2019**, *163*, 195.
- [58] X. Wei, Q. Gao, C. Xie, C. Gu, T. Liang, H. Wan, L. Zhuang, Y. He, P. Wang, *Anal. Methods* **2019**, *11*, 5872.
- [59] Z. Hao, S. Wang, J. Nie, D. Li, A. Fang, J. Kang, C. Liu, L. Wang, *Bio-des. Manuf.* **2021**, *4*, 33.
- [60] Y. Ye, F. Jiang, *Nano Energy* **2022**, *99*, 107374.
- [61] B. Khan, S. Abdullah, S. Khan, *Micromachines* **2023**, *14*, 1005.
- [62] J. A. Sánchez-Fernández, G. Presbítero-Espinosa, L. Peña-Parás, E. I. R. Pizaña, K. P. V. Galván, M. Vopálský, I. Kumpová, L. E. Elizalde-Herrera, *Polymers* **2021**, *13*, 2927.
- [63] G. Zhang, T. Guan, J. Zhang, T. Zhang, *J. Food Sci.* **2021**, *86*, 434.
- [64] J. Chen, A. Wu, M. Yang, Y. Ge, P. Pristijono, J. Li, B. Xu, H. Mi, *Food Control* **2021**, *126*, 108063.
- [65] A. Georgopoulou, B. Vanderborcht, F. Clemens, *Front. Rob. AI* **2021**, *8*, 326.
- [66] A. Georgopoulou, F. Clemens, *Flexible Printed Electron.* **2022**, *7*, 025010.
- [67] C. J. Wright, B. Z. Molino, J. H. Y. Chung, J. T. Pannell, M. Kuester, P. J. Molino, T. W. Hanks, *Gels* **2020**, *6*, 13.

- [68] F. Freeman, D. Kelly, *Sci. Rep.* **2017**, *7*, 17042.
- [69] M. Temirel, C. Hawxhurst, S. Tasoglu, *Micromachines* **2021**, *12*, 195.
- [70] B. Blanco-Fernandez, S. Rey-Vinolas, G. Bağci, G. Rubí, J. Otero, D. Navajas, S. Perez-Amodio, E. Engel, *ACS Appl. Mater. Interfaces* **2022**, *14*, 2946.
- [71] A. Prasopthum, Z. Deng, I. M. Khan, Z. Yin, B. Guo, J. Yang, *Biomater. Sci.* **2020**, *8*, 4287.
- [72] S. Vijayavenkataraman, S. Kannan, T. Cao, J. Y. H. Fuh, G. Sriram, W. F. Lu, *Front. Bioeng. Biotechnol.* **2019**, *7*, 266.